

# Hydrodynamic turbulence in quasi-Keplerian rotating flows

Liang Shi,<sup>1,2,\*</sup> Björn Hof,<sup>1,3</sup> Markus Rampp,<sup>4</sup> and Marc Avila<sup>5,6,†</sup>

<sup>1</sup>*Max Planck Institute for Dynamics and Self-Organization (MPIDS), 37077 Göttingen, Germany*

<sup>2</sup>*Institute of Geophysics, University of Göttingen, 37077 Göttingen, Germany*

<sup>3</sup>*Institute of Science and Technology Austria, 3400 Klosterneuburg, Austria*

<sup>4</sup>*Max Planck Computing and Data Facility, Gießenbachstr. 2, 85748 Garching, Germany*

<sup>5</sup>*Institute of Fluid Mechanics, Friedrich-Alexander-Universität Erlangen-Nürnberg, 91058 Erlangen, Germany*

<sup>6</sup>*Center of Applied Space Technology and Microgravity, University of Bremen, 28359 Bremen, Germany*

(Dated: December 14, 2024)

We report a direct-numerical-simulation study of Taylor-Couette flow in the quasi-Keplerian regime at shear Reynolds numbers up to  $\mathcal{O}(10^5)$ . Quasi-Keplerian rotating flow has been investigated for decades as a simplified model system to study the origin of turbulence in accretion disks that is not fully understood. The flow in this study is axially periodic and thus the experimental end-wall effects on the stability of the flow are avoided. Using optimal linear perturbations as initial conditions, our simulations find no sustained turbulence: the strong initial perturbations distort the velocity profile and trigger turbulence that eventually decays.

## I. INTRODUCTION

In protoplanetary disks the inward accretion of matter is accompanied by an outward transport of angular momentum. In case of laminar flow the momentum transport is solely governed by the fluid's molecular viscosity,  $\nu$ . The magnitude of the molecular viscosity is however much too small to account for the actually observed accretion rates. This discrepancy can be simply resolved by assuming that flows are turbulent which would considerably enhance the momentum transport. While the extremely large Reynolds numbers in such disks may be regarded as a justification for turbulence to occur, from a hydrodynamic stability perspective the situation is less clear. Disk flows have a Keplerian velocity profile with  $\Omega(r) \sim r^{-3/2}$ , where  $\Omega$  is the angular velocity. Such profiles are linearly stable according to the inviscid Rayleigh criterion [1] and no purely hydrodynamic instability mechanism is known that would provide a direct path to turbulence. In hot ionized disks on the other hand turbulence can be triggered by the so-called magnetorotational instability [2–4], but this is thought to be of lesser importance in cold and weakly ionized disks. For the latter case alternative mechanisms have been suggested as potential sources of turbulence. Especially concerning density gradients several instabilities have been proposed in the literature (stratorotational instability [5, 6]; Zombie vortex instability [7]; Rossby wave instability [8]; baroclinic instability [9]). Nevertheless, even in the absence of such instability mechanisms turbulence could potentially arise from a nonlinear (subcritical) instability. Subcritical instabilities are for instance responsible for turbulence in pipe and related shear flows. Whether such a scenario is also responsible for turbulence in quasi-Keplerian rotating flows remains unclear.

This question has been recently studied in experiments of fluid flows between co-rotating cylinders, Taylor-Couette flow (TCf). By selecting appropriate rotation rates (corotation with a faster inner cylinder) velocity profiles can be established that have stability properties similar to Keplerian flows. Like in Keplerian flows, the angular velocity decreases outwards while the angular momentum increases and the flow is Rayleigh stable. For this flow, Ji and co-workers [10, 11] have measured the Reynolds stress or the  $\beta$  parameter introduced by Richard and Zahn [12] at discrete interior locations, and at Reynolds numbers (Re) up to  $2 \times 10^6$ . They found that the experimentally measured  $\beta$  is consistent with laminar flows and thus far below the value inferred from astrophysical observations. These authors concluded that hydrodynamic turbulence cannot account for the expected transport rate of angular momentum in disks. This was challenged by the experimental results of Paoletti et al. [13, 14], who reported turbulent angular momentum transport in quasi-Keplerian TCf for Re above  $10^5$ . Their estimated  $\beta$  based on Torque measurements at the inner cylinder was found at similar level as in astrophysical disks. These contradictory conclusions are thought to arise because of design differences in the experiments, such as geometry (axial-length-to-gap aspect ratio  $\Gamma$ , and radius ratio  $\eta$ ) and end-cap treatment as well as the measured physical quantities, making comparison difficult [15].

In the experiments of Ji and co-workers [10, 11], the axial end walls were split into two independently rotating parts, whose rotation was selected as to minimize their effect on the bulk of the flow. The effectiveness of this strategy

---

\*Electronic address: Email address: gliang.shi@gmail.com

†Electronic address: Email address: marc.avila@zarm.uni-bremen.de

was demonstrated by Obabko *et al.* [16], who performed direct numerical simulation (DNS) of the same geometry and tested several different boundary conditions. In contrast, Paoletti *et al.* [13, 14] used a larger aspect ratio  $\Gamma = 11.47$  and measured the torque only around the mid-height of the experiment to avoid torque contributions arising near the end walls. However, their end walls were attached to the outer cylinder thereby generating a very strong Ekman circulation, which was shown to entirely fill the apparatus unless  $\Gamma \gg 100$  were used [17, 18].

Numerical simulations [19] precisely reproducing the geometry and boundary conditions of the two aforementioned experimental setups [10, 13] showed that the axial end walls strongly disrupt quasi-Keplerian velocity profiles and cause turbulence to arise for  $Re$  as low as  $\mathcal{O}(10^3)$ . Although this explains why strong turbulence is found in the experiments of Paoletti *et al.* [13, 14], as demonstrated later by the direct measurement of azimuthal velocity profiles performed by Nordsiek *et al.* [20], it still appears to be in contradiction with the results of Ji and co-workers [10, 11]. However, similar measurements performed by Edlund and Ji [21] compellingly show that if the end wall boundary conditions are optimally chosen, end-wall effects remain confined close to the axial boundaries and ideal laminar Couette profiles are obtained in the bulk of the experiments at sufficiently large  $Re$ . This was recently confirmed by direct numerical simulations of these experiments, which elucidated the progressive localization of turbulence at boundaries as  $Re$  increases up to  $5 \times 10^4$  [22].

Ostilla-Mónico *et al.* [23] performed direct numerical simulations of TCf with axially periodic cylinders thereby eliminating end-wall effects. Their initial conditions were turbulent states obtained for stationary outer cylinder (Rayleigh-unstable regime) and at  $t = 0$  the rotation of the cylinders was suddenly changed to quasi-Keplerian (by impulsively increasing the rotation of the outer cylinder). Their simulations showed an immediate direct decay of turbulence in agreement with the experiments of Edlund and Ji [21]. Note however, that sudden changes in the driving velocity can also cause laminarization of flows that are turbulent if appropriately disturbed [24]. Further, while for stationary outer cylinder the dominant flow features are turbulent (toroidal) Taylor vortices rooted on the linear stability of the laminar flow [25], in quasi-Keplerian flows the disturbance with highest transient energy growth are (axially invariant) Taylor columns [26, 27]. These two issues raise the question of whether the initial conditions used by Ostilla-Mónico *et al.* [23] and Lesur and Longaretti [28] are well suited as a trigger for turbulence in quasi-Keplerian flows. Following previous work on secondary instabilities [29–31] we perform direct numerical simulations of TCf with axially periodic cylinders starting from optimal perturbations superposed with very small three-dimensional random noise. Note that secondary means here that the laminar profile needs to be first disturbed with a “primary” disturbance so that random noise can grow exponentially like in a linear instability. Our approach is also similar to the experiments of Edlund and Ji [21], who apply strong injection disturbances to their quasi-Keplerian flow. Our simulations show transition to turbulence followed by its immediate decay at shear Reynolds number up to  $10^5$ .

## II. QUASI-KEPLERIAN TAYLOR–COUETTE FLOW

Figure 1 shows a sketch of the geometry of TCf, the flow between two independently rotating concentric cylinders. The inner (outer) cylinder has radius  $r_i$  ( $r_o$ ) and rotates at a speed of  $\Omega_i$  ( $\Omega_o$ ). The Reynolds numbers of the inner and outer cylinder are defined as  $Re_{i(o)} = \Omega_{i(o)} r_{i(o)} d / \nu$ , where  $d = r_o - r_i$  is the gap between the cylinders. The advective time unit,  $\tau_d = d / (r_i \Omega_i)$ , based on the velocity of the inner cylinder is used in this paper. The geometry of TCf is fully specified by two dimensionless parameters: the radius-ratio  $\eta = r_i / r_o$  and the length-to-gap aspect-ratio  $\Gamma = L_z / d$ , where  $L_z$  is the axial length of the cylinders. The angular velocity of the laminar base flow, called circular Couette flow, is given by

$$\Omega^b(r) = C_1 + \frac{C_2}{r^2},$$

$$\text{with } C_1 = \frac{Re_o - \eta Re_i}{1 + \eta}, \quad C_2 = \frac{\eta(Re_i - \eta Re_o)}{(1 - \eta)(1 - \eta^2)}, \quad (1)$$

which corresponds to a pure rotary shear flow.

The dimensionless parameter choice introduced by Dubrulle *et al.* [32] is very useful as it separates rotation from shear

$$Re_s = \frac{2}{1 + \eta} |\eta Re_o - Re_i|,$$

$$R_\Omega = \frac{(1 - \eta)(Re_i + Re_o)}{\eta Re_o - Re_i}. \quad (2)$$

The shear Reynolds number  $Re_s$  characterizes the shear between the inner and outer cylinders and is essentially the square of the Taylor number, whereas the rotation number  $R_\Omega$  is a measure for the mean rotation and is constant on

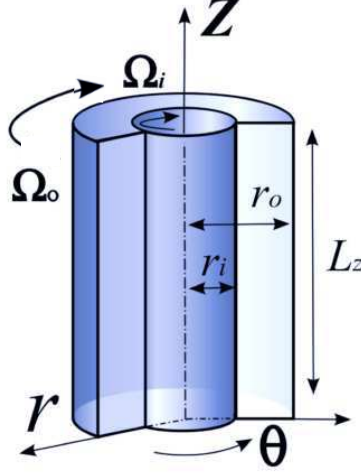


FIG. 1: Sketch of the geometry of Taylor-Couette flow (TCf) in cylindrical coordinates. The inner and outer cylinders of radii  $r_i$  and  $r_o$  rotate independently at a speed of  $\Omega_i$  and  $\Omega_o$ , respectively. No-slip boundary conditions at the cylinders are used together with axially periodic boundary conditions. The fluid between the cylinders is driven by the shear force due to the molecular viscosity.

every half-line out from the origin in the  $(Re_o, Re_i)$ -space (see Fig. 2). On the solid-body line, there is no relative motions between different layers and hence  $Re_s = 0$ , whereas  $R_\Omega = \pm\infty$ . The quasi-Keplerian regime in TCf is the co-rotation region limited by the Rayleigh line and the solid-body line in the  $(Re_o, Re_i)$  parameter space (the blue region in Fig. 2). The Rayleigh line ( $Re_o = \eta Re_i$ ) separates linearly stable and unstable inviscid fluid flows. Below the Rayleigh line, the circular Couette flow is linearly stable. On the solid-body line,  $\Omega_i = \Omega_o$  or  $Re_i = \eta Re_o$ , the fluids behave like a rigid body without shear, which means that all disturbances to the flow decay monotonically in time. In the quasi-Keplerian regime, the base velocity profiles satisfy two conditions: (1) radially increasing angular momentum  $d(\Omega^b(r)r^2)/dr > 0$ ; (2) radially decreasing angular velocity  $d\Omega^b(r)/dr < 0$ .

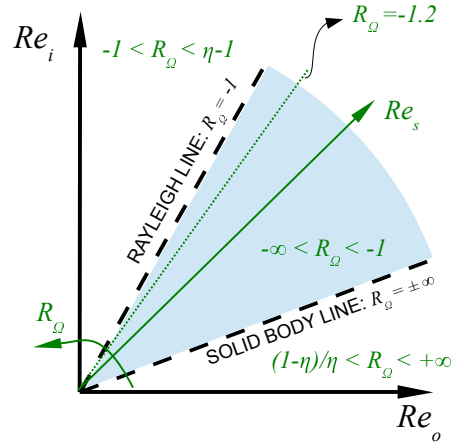


FIG. 2: The parameter space  $(Re_o, Re_i)$ . The blue region represents the quasi-Keplerian regime. The rotation number  $R_\Omega$  is constant along half-lines starting from origin. The ranges of  $R_\Omega$  are shown in different regions separated by the Rayleigh line ( $R_\Omega = -1$ ) and the solid body line ( $R_\Omega = \pm\infty$ ). The dotted line corresponds to the line  $R_\Omega = -1.2$ , on which our simulations are performed.

### III. NUMERICAL SPECIFICATION

Our direct numerical simulations were performed at four different Reynolds numbers  $Re_i = [1 \times 10^4, 2 \times 10^4, 1 \times 10^5, 2 \times 10^5]$  on the half line  $R_\Omega = -1.2$ , i.e., very close to the Rayleigh line  $R_\Omega = -1$ . This choice is motivated by Lesur and Longaretti [28], who speculated that if there were a subcritical transition, this might be easier to trigger near the stability boundary. The corresponding shear Reynolds numbers are  $Re_s = [5078.8, 10157.6, 50788, 101576]$ . In order to compare with recent experimental and numerical results, the radius ratio is chosen to be  $\eta = 0.71$ . Another relevant parameter often used in the astrophysical literature is the local exponent of the angular velocity  $q = -d\ln\Omega/d\ln r$ . For a Keplerian velocity profile,  $q = 3/2$ , and on the Rayleigh line  $q = 2$ . Note that for circular Couette flow the parameter  $q$  is not constant in the radial direction. In our simulations  $q(r) = \frac{2C_2}{C_1 r^2 + C_2} \in [1.5, 1.8]$ , which is in the quasi-Keplerian regime. A brief comparison between astrophysical Keplerian flow and TCf of our simulations is shown in table I.

	$\Omega^b(r)$	$Re_s$	$R_\Omega$	$q(r)$	axial boundary
TCf	$C_1 r + C_2/r$	$10^{4-5}$	-1.2	[1.5, 1.8]	periodic
Keplerian	$C r^{-3/2}$	$\gg 10^6$	-4/3	3/2	free surfaces

TABLE I: A parameter comparison between TCf of our study and astrophysical Keplerian flows: base angular velocity profile  $\Omega^b(r)$ , shear Reynolds number  $Re_s$ , rotation number  $R_\Omega$ , local exponent  $q(r)$  and axial boundary conditions.  $C_1$  and  $C_2$  are defined in Eq. (1) while  $C$  is another constant.

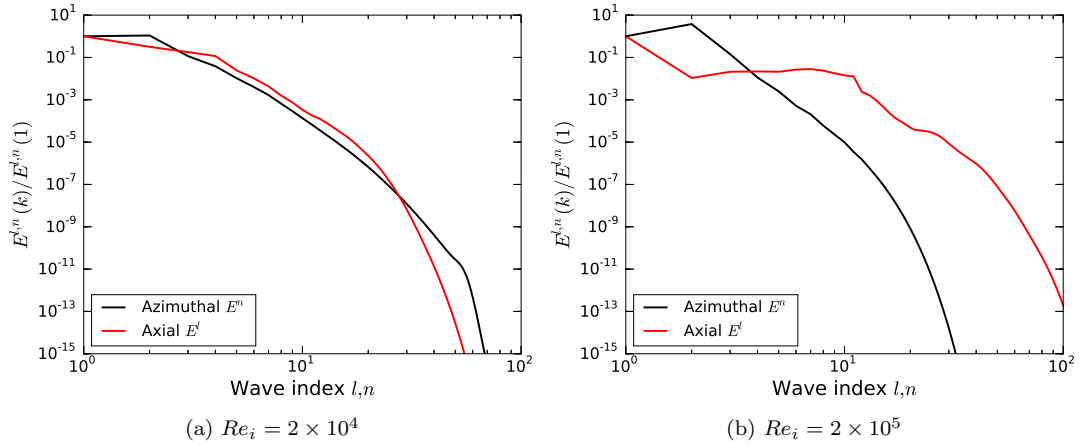


FIG. 3: Normalized axial (black) and azimuthal (red) energy power spectra  $E^{l,n}(k)$  for (a)  $Re_i = 2 \times 10^4$  at time  $t/\tau_d = 30$  and for (b)  $Re_i = 2 \times 10^5$  at time  $t/\tau_d = 35$ , before the decay of turbulence. Here  $l$  and  $n$  are the wave indices in the axial and azimuthal directions, respectively. The corresponding wavenumbers are  $l k_z$  and  $n k_\theta$ .

For the simulations we employ our parallel code `nsCouette` [33] which uses a spectral Fourier-Galerkin method for the discretization of the Navier-Stokes equation in the axial and azimuthal directions, and high-order finite differences in the radial direction, together with a second-order, semi-implicit projection scheme for the time integration, and employs a pseudospectral method for the evaluation of the nonlinear terms. The corresponding parameters of the simulations are listed in table II. At  $Re_i = 10^4$  we simulate a quarter of the cylinder in the azimuthal direction, corresponding to a basic azimuthal wavenumber  $k_\theta = 4/r_{mid}$ , with  $r_{mid} = 0.5(1 + \eta)/(1 - \eta)$ , and set  $\Gamma = L_z/d = 0.5$ , corresponding to a basic axial wavenumber  $k_z = 4\pi$ . The total number of grid points before de-aliasing ( $N_r \times N_\theta \times N_z$ ) is  $(256 \times 512 \times 256)$ . To save computing time, the domain size at higher Reynolds numbers is chosen smaller,  $k_\theta = 8$  and 16 (the factor  $1/r_{mid}$  is hereafter omitted for simplicity), at  $Re_i = 10^5$  and  $Re_i = 2 \times 10^5$ , respectively. As shown in [34, 35], a reduction of the domain length in the azimuthal direction has little effect on the statistical properties of the simulated turbulent flows, as long as the dominant structures are still captured. At high  $Re$  the spatial resolution in each direction is increased approximately as  $N \sim Re^{3/4}$ , given that the domain size is the same. The resolution is checked at  $Re_i = 2 \times 10^4$  and  $Re_i = 2 \times 10^5$  by the axial and azimuthal energy spectra as a function of the wave index  $l, n$  (see Fig. 3). We should point out that in the case III a lower resolution than the one shown in Table II causes the simulations to blow up. This may be explained by the fact that with a low resolution the scales at which

energy dissipates is not resolved so that the energy accumulates in the flow and causes the simulations to diverge.

No.	$Re_i$	$Re_s$	$k_\theta$	# points	$dt/\tau_d$
I	$1 \times 10^4$	5078.8	4	$256 \times 512 \times 256$	$10^{-5}$
II	$2 \times 10^4$	10157.6	8	$256 \times 512 \times 256$	$2 \times 10^{-5}$
III	$1 \times 10^5$	50788	16	$1152 \times 384 \times 384$	$10^{-4}$
IV	$2 \times 10^5$	101576	16	$2048 \times 768 \times 512$	$10^{-4}$

TABLE II: DNS parameters of TCf in the quasi-Keplerian regime. The radius ratio is  $\eta = 0.71$  and the length-to-gap aspect ratio in the axially periodic direction is  $\Gamma = 0.5$ .

Our initial conditions are optimal perturbations from the computations of the transient growth by Maretzke et al. [26], on top of which small three dimensional random noise exciting axial modes  $l = 1, \dots, 10$  is added. The optimal perturbations are computed at fixed  $k_\theta$  (e.g.  $k_\theta = 4$  at  $Re_s = 10^4$ ) and hence are optimal only in their subspace. Using the full domain in the azimuthal direction ( $k_\theta = 1$ ) would yield slightly higher transient growth. In all cases the azimuthal wavenumber of the optimal perturbation is chosen to be the same as the basic azimuthal wavenumber fixing the domain length in the azimuthal direction. For the case  $R_\Omega = -1.2$  and  $Re_s > \mathcal{O}(10^3)$ , the optimal axial wavenumber is  $k_z = 0$ , corresponding to an axially-invariant Taylor-column-like structure. In the  $r - \theta$  plane, the optimal perturbation has an elongated spiral structure, similar to Fig. 8(a) in [26], and extracts energy from the basic flow via the Orr mechanism. The optimal transient growth energy values, denoted as  $G^{\text{opt}}$  (the mathematical definition can be found in [26]), at the investigated Reynolds numbers are listed in table III.

The initial velocity field  $\mathbf{u}_0$  is composed of three parts: the base flow  $\mathbf{U}_b$ , the 2D optimal perturbation  $\mathbf{u}_0^{2D}$  and the 3D noise  $\mathbf{u}_0^{3D}$ :  $\mathbf{u}_0 = \mathbf{U}_b + \mathbf{u}_0^{2D} + \mathbf{u}_0^{3D}$ . The relative magnitude of the amplitude of the three components is  $\|\mathbf{U}_b\| \gg \|\mathbf{u}_0^{2D}\| \gg \|\mathbf{u}_0^{3D}\|$ . The simulations are computationally expensive: simulation IV, for example, was performed on the high-performance system Hydra at the Max Planck Computing and Data Facility and required about  $5 \times 10^6$  core hours using 5120 cores utilized by 512 MPI tasks (2 tasks per 20-core-node) with 10 OpenMP threads each.

No.	$Re_i$	$k_z$	$k_\theta$	$G^{\text{opt}}$	$t^{\text{opt}}/\tau_d$
I	$1 \times 10^4$	0	4	13.04	27
II	$2 \times 10^4$	0	8	24.40	22
III	$1 \times 10^5$	0	8	73.98	36
IV	$2 \times 10^5$	0	16	82.13	28

TABLE III: The transient growth rate of the initial perturbations attained at time  $t^{\text{opt}}$  and their corresponding wavenumbers.

We use the total perturbation kinetic energy as a diagnostic quantity. Assuming that  $\hat{\mathbf{u}}^{ln}(r) = \hat{\mathbf{u}}(r, lk_\theta, nk_z)$  are the spectral coefficients in Fourier space of the velocity field  $\mathbf{u}(r, \theta, z)$ , the modal kinetic energy density  $E^{ln}$  associated with the Fourier mode  $(l, n)$  is defined as

$$E^{ln} = \frac{1}{2} \int_{r_i}^{r_o} [\hat{u}_r^{ln}(r)^2 + \hat{u}_\theta^{ln}(r)^2 + \hat{u}_z^{ln}(r)^2] r dr. \quad (3)$$

We also analyze the contributions of the kinetic energy of the axial mode  $l$  and of the azimuthal mode  $n$ , respectively,

$$E^l = \sum_{n=-N}^N E^{ln}, \quad E^n = \sum_{l=-L}^L E^{ln}. \quad (4)$$

The total kinetic energy can therefore be expressed as

$$E = \sum_{l=-L}^L \sum_{n=-N}^N E^{ln}. \quad (5)$$

By removing the laminar part from the total energy we obtain the perturbation energy  $E_p$ , which is defined according to Eq. 3 but replacing  $\hat{u}_\theta^{00}(r)$  with  $[\hat{u}_\theta^{00}(r) - U_\theta^b(r)]$ . Note that the spectral coefficient at  $l = 0$  and  $n = 0$ ,  $\hat{u}_\theta^{00}(r)$ , is the average azimuthal velocity.

## IV. RESULTS

### A. Nonlinear transient growth

The behavior of the transient growth of the initial 2D optimal perturbation at  $Re_i = 10^4$  and  $k_\theta = 4$  is first investigated. Two groups of simulations were performed: with and without 3D noise. Let  $A^{2D}$  and  $A^{3D}$  denote the relative amplitude of 2D perturbation and 3D noise, scaled by the inner Reynolds number  $Re_i$  (the circular Couette flow).  $A^{2D} = 10^{-4}$  means that the absolute amplitude of the 2D perturbation is  $10^{-4} \times Re_i = 1$ . In order to test the effect of nonlinear terms, two runs with different relative 2D amplitude  $A^{2D} = 10^{-4}, 10^{-2}$  and without noise have been

conducted. The time evolution of the perturbation kinetic energy normalized by the initial value is shown in Fig. 4 (dashed lines). At low perturbation amplitude  $A^{2D} = 10^{-4}$  the maximum amplification  $G^{\text{opt}} = 13.04$  is attained at  $t/\tau_d = 27$ , in excellent agreement with the linear prediction (see Table III). With an amplitude  $A^{2D} = 10^{-2}$ , the transient growth rate is slightly reduced due to the non-negligible nonlinear effects. When adding noise similar transient growth behavior is found, see Fig. 4 (solid lines). Because of the negligible nonlinear effect, the added 3D noise decays monotonically to zero and seems to have no influence on the dynamics of 2D optimal perturbations.

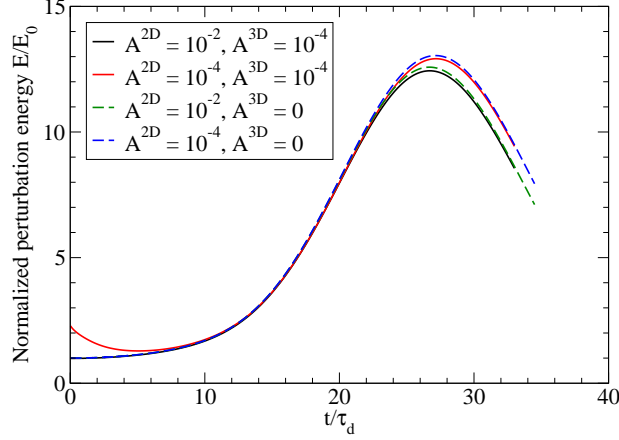


FIG. 4: The nonlinear evolution of the perturbation kinetic energy normalized by the initial energy of the 2D perturbation and 3D noise at  $Re_i = 10^4$ . Dashed lines: Without 3D noise, i.e.,  $A^{3D} = 0$ ; Solid lines: With 3D noise, excited from  $k_z = 1, \dots, 10$ . The relative amplitude of the 3D noise is  $A^{3D} = 10^{-4}$ , normalized by the inner Reynolds number  $Re_i$ . Colors indicate different relative 2D amplitudes.

### B. Transition and decay of turbulence

By increasing the amplitude of the 2D perturbations or 3D noise above a certain level, nonlinear effects become important and qualitatively change the dynamics of the flow. This has been observed at all Reynolds numbers investigated, and we first focus on the results at  $Re_i = 2 \times 10^4$  using  $k_\theta = 8$ , for which the transient growth of the 2D optimal perturbation is  $G^{\text{opt}} = 24.4$ , attained at  $t/\tau_d = 22$ . Here, four runs have been performed, based on different relative amplitudes of 2D perturbations and 3D noise:

1.  $A^{2D} = 5 \times 10^{-3}, A^{3D} = 5 \times 10^{-6}$
2.  $A^{2D} = 5 \times 10^{-2}, A^{3D} = 5 \times 10^{-6}$
3.  $A^{2D} = 5 \times 10^{-2}, A^{3D} = 5 \times 10^{-5}$
4.  $A^{2D} = 5 \times 10^{-2}, A^{3D} = 5 \times 10^{-4}$

The temporal evolution of the normalized perturbation kinetic energy for all these cases is shown in the top panel of Fig. 5. Interestingly, the flow dynamics for  $A^{2D} = 5 \times 10^{-3}$  and  $A^{2D} = 5 \times 10^{-2}$  are qualitatively different. At lower amplitude  $A^{2D} = 5 \times 10^{-3}$ , the flow basically follows the path of the linear transient growth, with a maximum of about 24.15 at  $t/\tau_d = 22$ , followed by an exponential decay. However, at  $A^{2D} = 5 \times 10^{-2}$ , a second “peak” or “bump” appears after the initial transient growth, especially for the cases with larger 3D noise. In addition, the transient growth is reduced and occurs earlier if the level of 3D noise is large. The reason behind this qualitatively different behaviour at  $A^{2D} = 5 \times 10^{-3}$  and  $A^{2D} = 5 \times 10^{-2}$  is apparent in Fig. 6, where the axial modal kinetic energy  $E^n(t)$  is shown. In both cases, the mode  $k_z = 0$  shows the initial transient growth as predicted by linear analysis. However, at the initial stage, the higher axial energy modes for  $A^{2D} = 5 \times 10^{-2}$  experience exponential or even faster growth, whereas for  $A^{2D} = 5 \times 10^{-3}$  they all decay.

At  $Re_i = 2 \times 10^5$  and  $k_\theta = 16$  simulations were done for  $A^{2D} = 2.5 \times 10^{-3}$  and  $A^{2D} = 5 \times 10^{-3}$ . The temporal evolution of the normalized perturbation kinetic energy is shown in the bottom panel of Fig. 5. At higher amplitude,

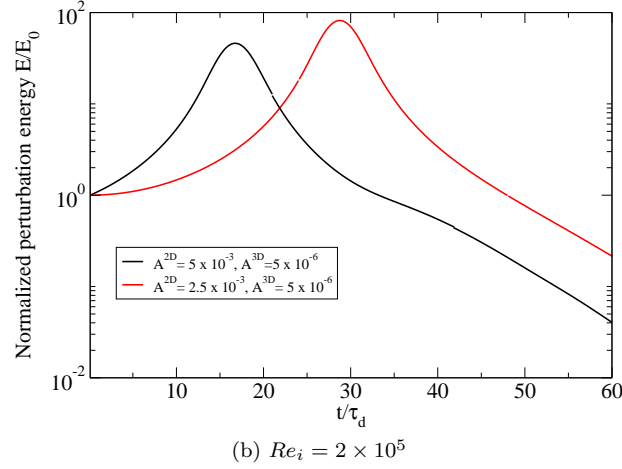
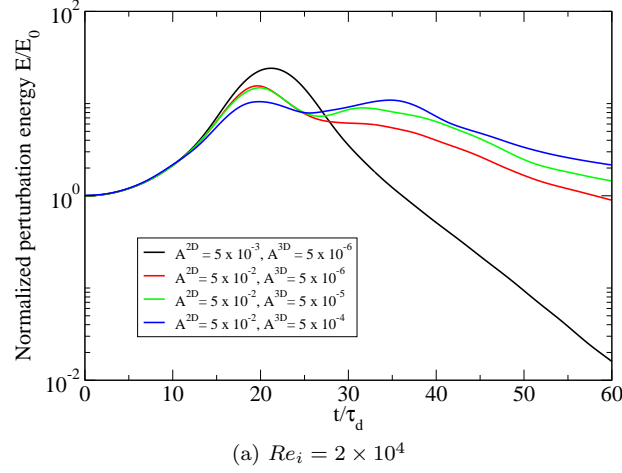


FIG. 5: The temporal evolution of the normalized perturbation kinetic energy at  $Re_i = 2 \times 10^4$  (a) and  $Re_i = 2 \times 10^5$  (b). The line colors correspond to different perturbation amplitudes.

the initial transient growth peak occurs at an earlier moment and its value is lower than the linear prediction, while at the lower amplitude the perturbation energy follows basically the linear dynamics (the same behavior is observed for  $Re_i = 10^5$ ). When we look at the evolution of the axial modal energy (Fig. 7), the difference is obvious, as has been found at  $Re_i = 2 \times 10^4$ . At higher perturbation amplitude, the exponential growth of higher axial modes turns the flow temporarily chaotic, but the ensuing turbulent motions finally decay and the flow returns to laminar. At  $Re_i = 2 \times 10^5$ , the modal energy is much higher due to stronger nonlinear interactions and the relaminarization process, which is controlled by viscosity, takes much longer when measured in advective time units. In summary, the following conclusions can be drawn.

1. At small perturbation amplitude nonlinear effects are negligible and the flow follows the linear dynamics.
2. At large enough perturbation amplitude, the initial maximum growth of the total energy is smaller and attained at an earlier moment.
3. Transition to turbulence occurs via three-dimensional secondary instabilities of the flow modified by the optimal disturbance [30].
4. The resulting hydrodynamic turbulence at  $Re_s$  up to  $10^5$  is not sustained and eventually decays.



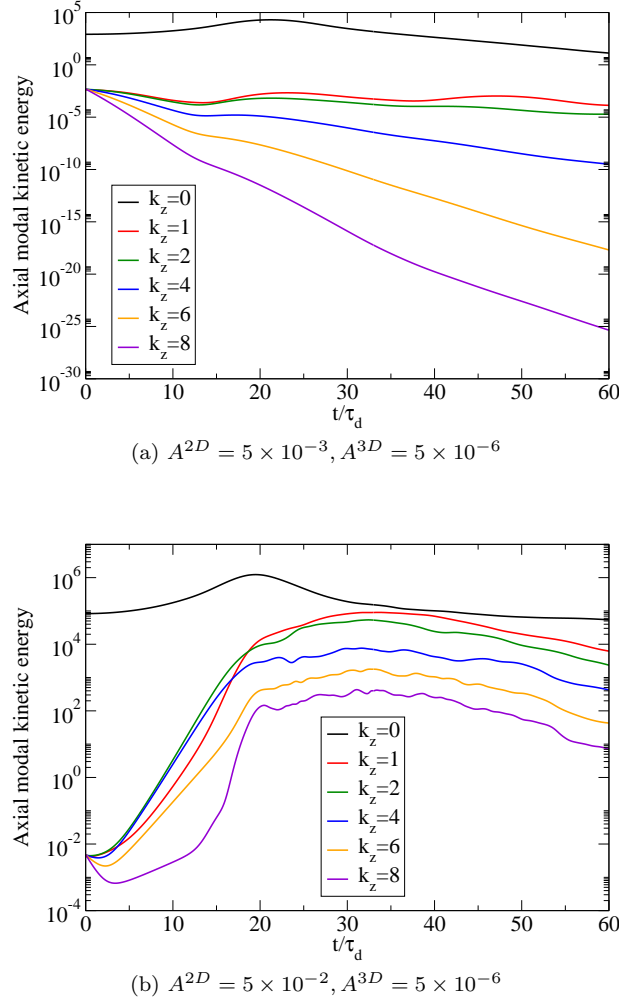


FIG. 6: The temporal evolution of the axial modal kinetic energy at  $Re_i = 2 \times 10^4$  for  $A^{2D} = 5 \times 10^{-3}, A^{3D} = 5 \times 10^{-6}$  (a), and  $A^{2D} = 5 \times 10^{-2}, A^{3D} = 5 \times 10^{-6}$  (b). The different lines correspond to different axial modes as indicated in the legend.

A remaining intriguing issue concerns the physical mechanism responsible for the two distinct behaviors at different perturbation amplitude as described above. Dubrulle and Knobloch [36] proposed that finite amplitude perturbations may generate inflection points in the base profile, which cause secondary instabilities and breakdown to turbulence. A similar mechanism was suggested in pipe flow by Meseguer [37], who performed simulations with different 2D and 3D perturbation amplitudes and observed sustained transition to turbulence at sufficiently large amplitudes. However, as shown in Fig. 8 (a, c), the perturbed azimuthal velocity profiles all have inflection points but some fail to generate turbulence. Moreover, one important difference with secondary instability as observed in non-rotating shear flows, such as channel, Couette and pipe flow is that the amplitude of the optimal mode needed to trigger the secondary instability is very high [38–40]. Figures 6 and 7 show that in fact the energy of the three-dimensional modes starts growing already at  $t = 0$  and not when the transient growth peaks. It is thus very unlikely that the transient growth is responsible for the observed transition. Instead it appears that at  $t = 0$  the base flow is already sufficiently distorted so that the flow is already linearly unstable. Figure 8 (b, d) shows the radial distribution of the angular momentum  $L(r) = (U_\theta^b + u_\theta^{2D})r$  at  $t = 0$  for  $Re_i = 2 \times 10^4$  and  $2 \times 10^5$ . The black curves correspond to runs in which no secondary instability is observed, whereas the red curves correspond to unstable runs. In the latter there are several regions in the flow in which the angular momentum decreases outwards, locally, and thus these regions are centrifugally unstable according to the Rayleigh criterion for inviscid rotating fluids. Figure 9 shows the instantaneous vertical velocity  $u_z$  at  $Re_i = 2 \times 10^4$  at four different instants of the time evolution. The horizontal planes show false-color plots of the radial derivatives of angular momentum  $dL/dr$ . There are regions in which the angular momentum decreases steeply, thereby suggesting that the instability is centrifugal in nature. The emerging streamwise vortices are nearly axisymmetric and are reminiscent of Taylor vortex flow. Note that the Rayleigh criterion is inviscid and viscosity has

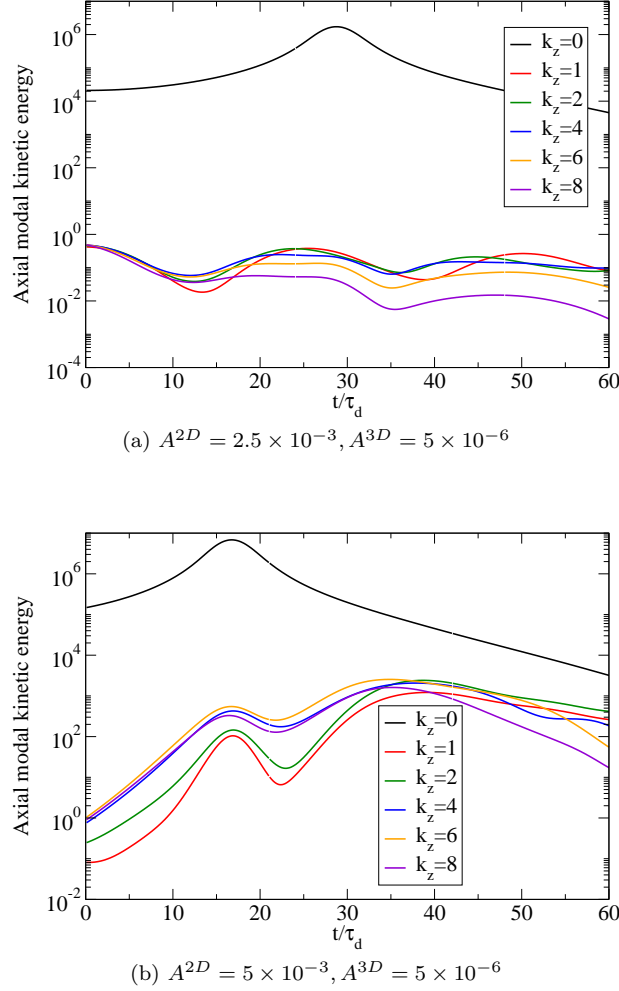


FIG. 7: The temporal evolution of the axial modal kinetic energy at  $Re_i = 2 \times 10^5$  for  $A^{2D} = 2.5 \times 10^{-3}, A^{3D} = 5 \times 10^{-6}$  (a) and  $A^{2D} = 5 \times 10^{-3}, A^{3D} = 5 \times 10^{-6}$  (b). Different colors correspond to different axial modes.

a stabilising effect, so that locally Rayleigh-unstable regions are not sufficient for flow instability to occur in viscous flows. In a Rayleigh-unstable region of length  $l$  the viscous (Laplacian) term in the Navier–Stokes equation implies that the stabilizing effect is proportional to  $1/l^2$ , so that the smaller  $l$  is, the larger the stabilising effect is. Hence in very small Rayleigh-unstable regions the instabilities are strongly suppressed by viscosity. Decaying turbulence is clearly observed at  $Re_i = 2 \times 10^5$ , where the flow is much more turbulent, as shown in the volume rendering of the streamwise vorticity in Fig. 10 (Multimedia view).

## V. CONCLUSION

We performed direct numerical simulations of axially periodic TCf in the quasi-Keplerian regime by strongly disturbing the laminar Couette flow. No sustained turbulence was found at shear Reynolds numbers up to  $\mathcal{O}(10^5)$ , in agreement with previous experiments (see Ref. [18] and references therein) and direct numerical simulations [23] using turbulent initial conditions. We used linear optimal perturbations (axially invariant Taylor columns) superposed with small three-dimensional noise. Depending on the initial perturbation amplitude, the flow dynamics vary significantly. At small amplitudes, the flow follows the path of linear transient growth, whereas at large initial amplitude the initial growth is reduced and the peak of the transient growth occurs at earlier times because of non-negligible nonlinear

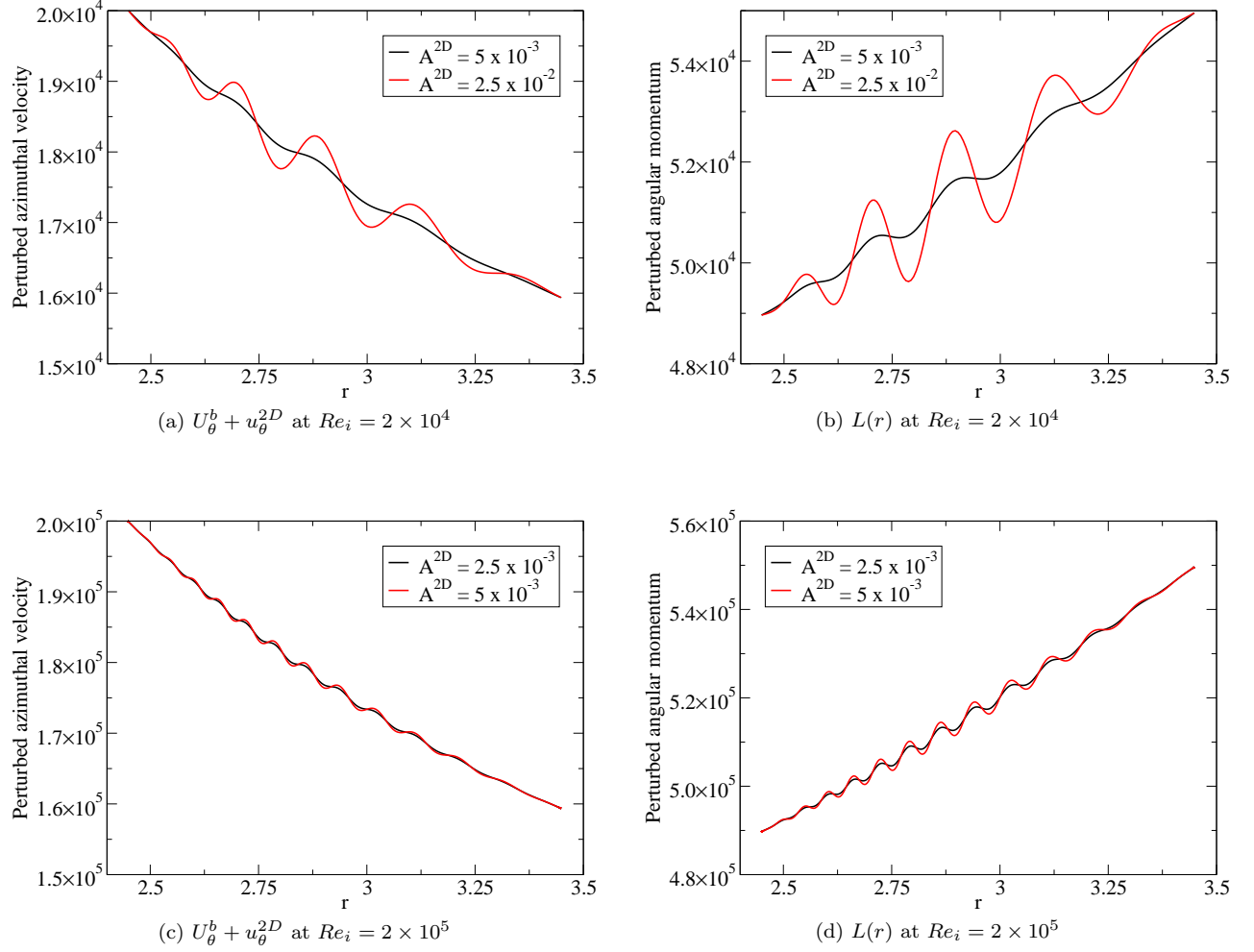


FIG. 8: Radial profiles of the perturbed azimuthal velocity (a, c) and Angular momentum  $L(r) = (U_\theta^b + u_\theta^{2D})r$  (b, d) at  $t = 0$  for  $Re_i = 2 \times 10^4$  (a, b) and  $Re_i = 2 \times 10^5$  (c, d).

effects. For sufficiently large amplitudes transition to turbulence can be triggered followed by rapid decay driven by viscous effects.

The transition scenario found here is qualitatively different from that in wall-bounded shear flows without rotation. In the latter optimal disturbances are stream-wise aligned vortices and when used as initial conditions they create velocity streaks, which render the flow linearly unstable and subsequently turbulent [41, 42]. This streak instability and the generation of streaks via stream-wise vortices are the essential ingredients for the self-sustenance of turbulence in wall-bounded shear flows [43, 44]. Instead, in quasi-Keplerian TCf stream-wise vortices are unable to efficiently extract energy from Couette flow [26], and so they cannot contribute to a self-sustaining process [45]. Here the optimal disturbances are axially invariant vortices, and their transient growth is substantially smaller than for stream-wise vortices in wall-bounded shear flows without rotation [26]. Our simulations indicate that these axially invariant disturbances cannot generate a secondary instability unless they are so large that they already initially, i.e. without energy growth, modify regions of the Couette flow so that these become locally Rayleigh unstable. This instability is unable to recreate the axially invariant optimal modes and so turbulence decays immediately after transition. Whether hydrodynamic turbulence can be sustained at even higher Reynolds number requires further research.

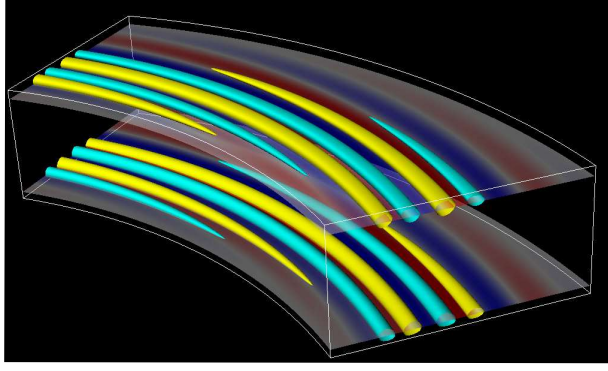
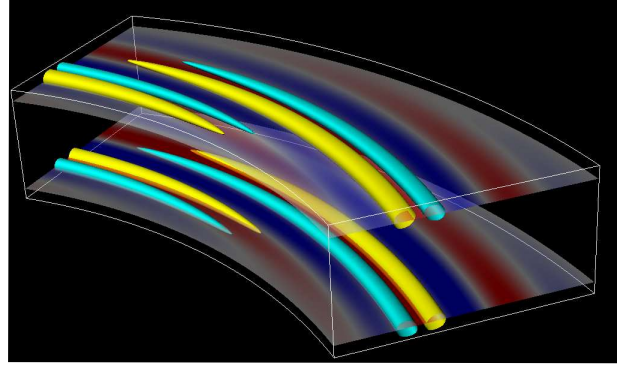
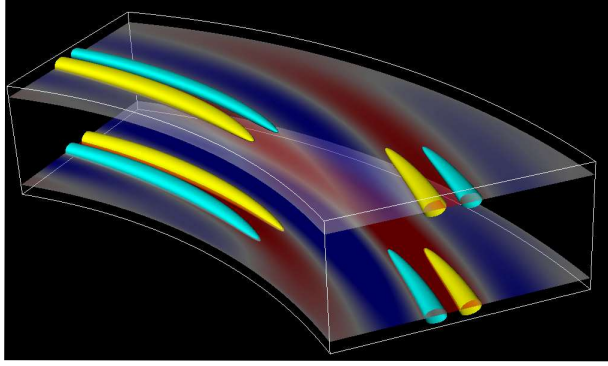
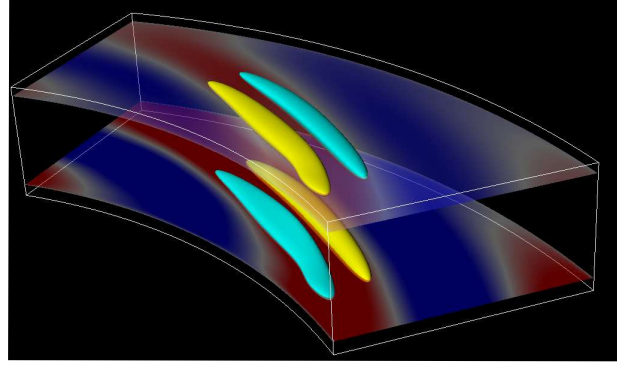
(a)  $t/\tau_d = 4$ (b)  $t/\tau_d = 8$ (c)  $t/\tau_d = 12$ (d)  $t/\tau_d = 16$ 

FIG. 9: Isosurfaces of the instantaneous vertical velocity  $u_z$  at  $Re_i = 2 \times 10^4$  for  $A^{2D} = 2.5 \times 10^{-2}$  and  $A^{3D} = 5 \times 10^{-6}$  at time  $t/\tau_d = 4$  (a),  $t/\tau_d = 8$  (b),  $t/\tau_d = 12$  (c) and  $t/\tau_d = 16$  (d). Two iso-levels are used: Yellow indicates positive  $u_z$  and cyan is for negative  $u_z$ . The two horizontal planes show the radial derivative of the angular momentum  $dL/dr$ . The (symmetric) colour scale varies from red (positive) over white (zero) to blue (negative).

#### Acknowledgement

L. Shi and B. Hof acknowledge research funding by the Deutsche Forschungsgemeinschaft (DFG, Germany) under grant No. SFB963/1 (Project A8). Computing time was allocated through the PRACE DECI-10 project HYDRAD and by the Max Planck Computing and Data Facility (Garching, Germany).

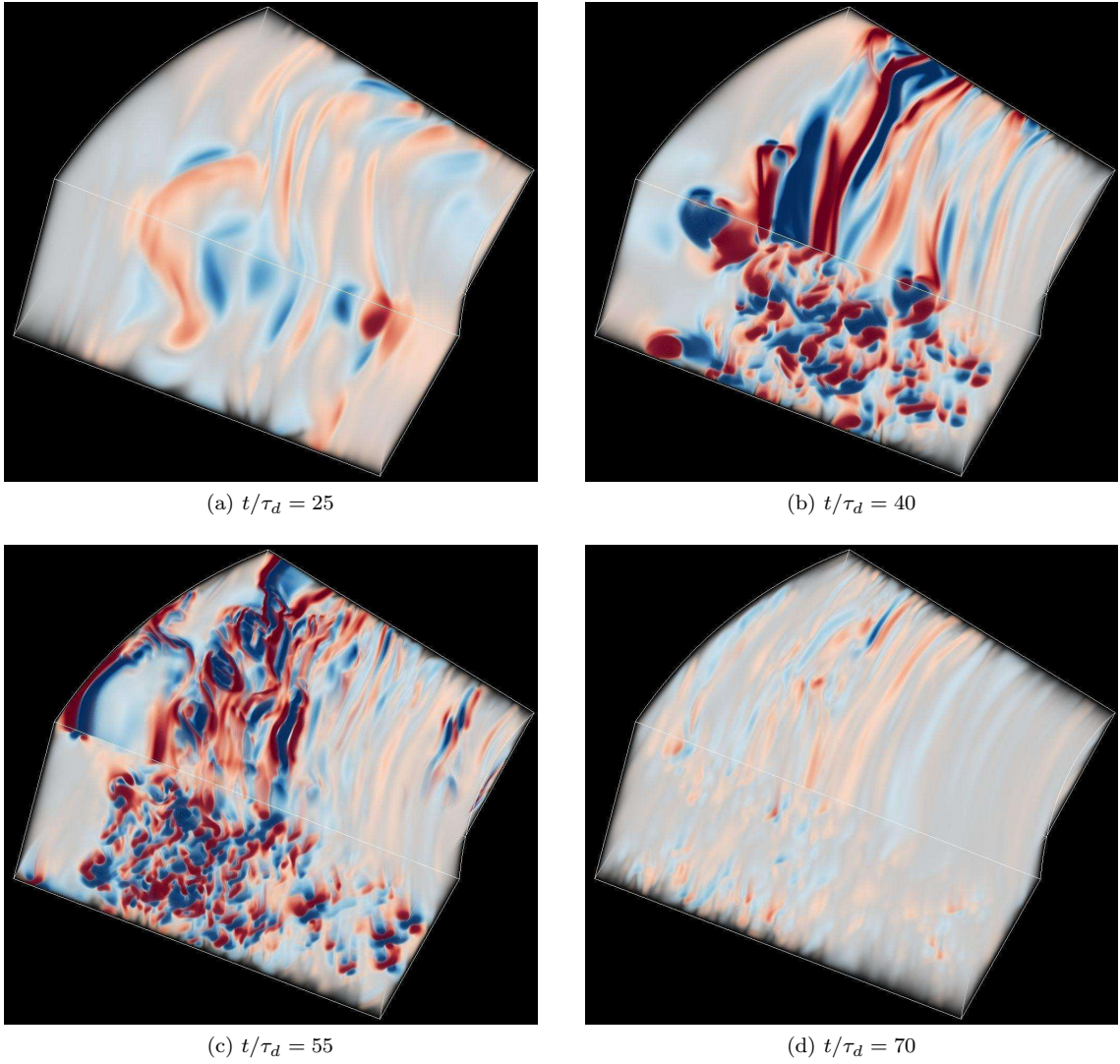


FIG. 10: Volume rendering of the instantaneous streamwise vorticity  $\omega_\theta$  at  $Re_i = 2 \times 10^5$  for  $A^{2D} = 5 \times 10^{-3}$  and  $A^{3D} = 5 \times 10^{-6}$  at times  $t/\tau_d = 25$  (a),  $t/\tau_d = 40$  (b),  $t/\tau_d = 55$  (c) and  $t/\tau_d = 70$  (d). Red (blue) colours trace regions with positive (negative)  $\omega_\theta$ . (Multimedia view)

- 
- [1] L. Rayleigh, Proc. R. Soc. Lond. A **93**, 148 (1917).
  - [2] S. A. Balbus and J. F. Hawley, Astron. Astrophys. **376**, 214 (1991).
  - [3] S. A. Balbus and J. F. Hawley, Rev. Mod. Phys. **70**, 1 (1998).
  - [4] S. A. Balbus, Annu. Rev. Astron. Astrophys. **41**, 555 (2003).
  - [5] D. Shalybkov and G. Rüdiger, Astron. Astrophys. **438**, 411 (2005).
  - [6] M. L. Bars and P. L. Gal, Phys. Rev. Lett. **99**, 064502 (2007).
  - [7] P. S. Marcus, S. Pei, C.-H. Jiang, J. A. Barranco, P. Hassanzadeh, and D. Lecoanet, Astrophys. J. **808**, 87 (2015).
  - [8] R. Lovelace, H. Li, S. Colgate, and A. Nelson, Astrophys. J. **513**, 805 (1999).
  - [9] H. H. Klahr and P. Bodenheimer, Astrophys. J. **582**, 869 (2003).
  - [10] H. Ji, M. J. Burin, E. Schartman, and J. Goodman, Nature **444**, 343 (2006).
  - [11] E. Schartman, H. Ji, M. J. Burin, and J. Goodman, Astron. Astrophys. **543**, A94 (2012).
  - [12] D. Richard and J.-P. Zahn, Astron. Astrophys. **347**, 734 (1999).
  - [13] M. S. Paoletti and D. P. Lathrop, Phys. Rev. Lett. **106** (2011).
  - [14] M. S. Paoletti, D. P. M. van Gils, B. Dubrulle, C. Sun, D. Lohse, and D. P. Lathrop, Astron. Astrophys. **547**, A64 (2012).
  - [15] S. Balbus, Nature **470**, 475 (2011).
  - [16] A. V. Obabko, F. Cattaneo, and P. F. Fischer, Physica Scripta **2008**, 014029 (2008), URL

<http://stacks.iop.org/1402-4896/2008/i=T132/a=014029>.

- [17] R. Hollerbach and A. Fournier, MHC Couette Flows: Experiments and Models, ed. G. Rosner, G. Rüdiger & A. Bonanno, AIP Conference Proceedings **733**, 114 (2004).
- [18] E. M. Edlund and H. Ji, Phys. Rev. E **92**, 043005 (2015).
- [19] M. Avila, Phys. Rev. Lett. **108** (2012).
- [20] F. Nordsiek, S. G. Huisman, R. C. A. van der Veen, C. Sun, D. Lohse, and D. P. Lathrop, J. Fluid Mech. pp. 342–362 (2015).
- [21] E. M. Edlund and H. Ji, Phys. Rev. E **89**, 021004(R) (2014).
- [22] J. M. Lopez and M. Avila, arXiv:1608.05527 (2016).
- [23] R. O. Mónico, R. Verzicco, S. Grossman, and D. Lohse, J. Fluid Mech. **748**, R3 (2014).
- [24] B. Hof, A. de Lozar, M. Avila, X. Tu, and T. M. Schneider, Science **327** (2010).
- [25] S. Grossmann, D. Lohse, and C. Sun, Ann. Rev. Fluid Mech. **48**, 53 (2016).
- [26] S. Maretzke, B. Hof, and M. Avila, J. Fluid Mech. **742**, 254 (2014).
- [27] L. S. Tuckerman, J. Fluid Mech. **750**, 1 (2014).
- [28] G. Lesur and P. Y. Longaretti, Astron. Astrophys. **444**, 25 (2005).
- [29] S. A. Orszag and A. T. Patera, J. Fluid Mech. **128**, 347 (1983).
- [30] P. J. Schmid and D. S. Henningson, Stability and Transition in Shear Flows (Springer, 2001).
- [31] M. Högberg and D. S. H. Henningson, J. Fluid Mech. **368**, 339 (1998).
- [32] B. Dubrulle, O. Dauchot, F. Daviaud, P.-Y. Longaretti, D. Richard, and J.-P. Zahn, Phys. Fluids **17**, 095103 (2005).
- [33] L. Shi, M. Rampp, B. Hof, and M. Avila, Computers & Fluids **106**, 1 (2015).
- [34] H. J. Brauckmann and B. Eckhardt, J. Fluid Mech. **718**, 398 (2013).
- [35] R. O. Mónico, R. Verzicco, and D. Lohse, Phys. Fluids **27**, 025110 (2015).
- [36] B. Dubrulle and E. Knobloch, Astron. Astrophys. **256**, 673 (1992).
- [37] A. Meseguer, Phys. Fluids **15**, 1203 (2003).
- [38] A. G. Darbyshire and T. Mullin, J. Fluid Mech. **289**, 83 (1995).
- [39] O. Dauchot and F. Daviaud, Phys. Fluids **7**, 335 (1995).
- [40] B. Eckhardt, T. M. Schneider, B. Hof, and J. Westerweel, Ann. Rev. Fluid Mech. **39**, 447 (2007).
- [41] O. Y. Zikanov, Phys. Fluids **8**, 2923 (1996).
- [42] W. Schoppa and F. Hussain, J. Fluid Mech. **453**, 57 (2002).
- [43] J. M. Hamilton, J. Kim, and F. Waleffe, J. Fluid Mech. **287**, 317 (1995).
- [44] F. Waleffe, Phys. Fluids **9**, 883 (1997).
- [45] F. Rincon, G. I. Ogilvie, and C. Cossu, Astron. Astrophys. **463**, 817 (2007).